Journal of Materials Chemistry A

Materials for energy and sustainability

rsc.li/materials-a

ROYAL SOCIETY
OF **CHEMISTRY**
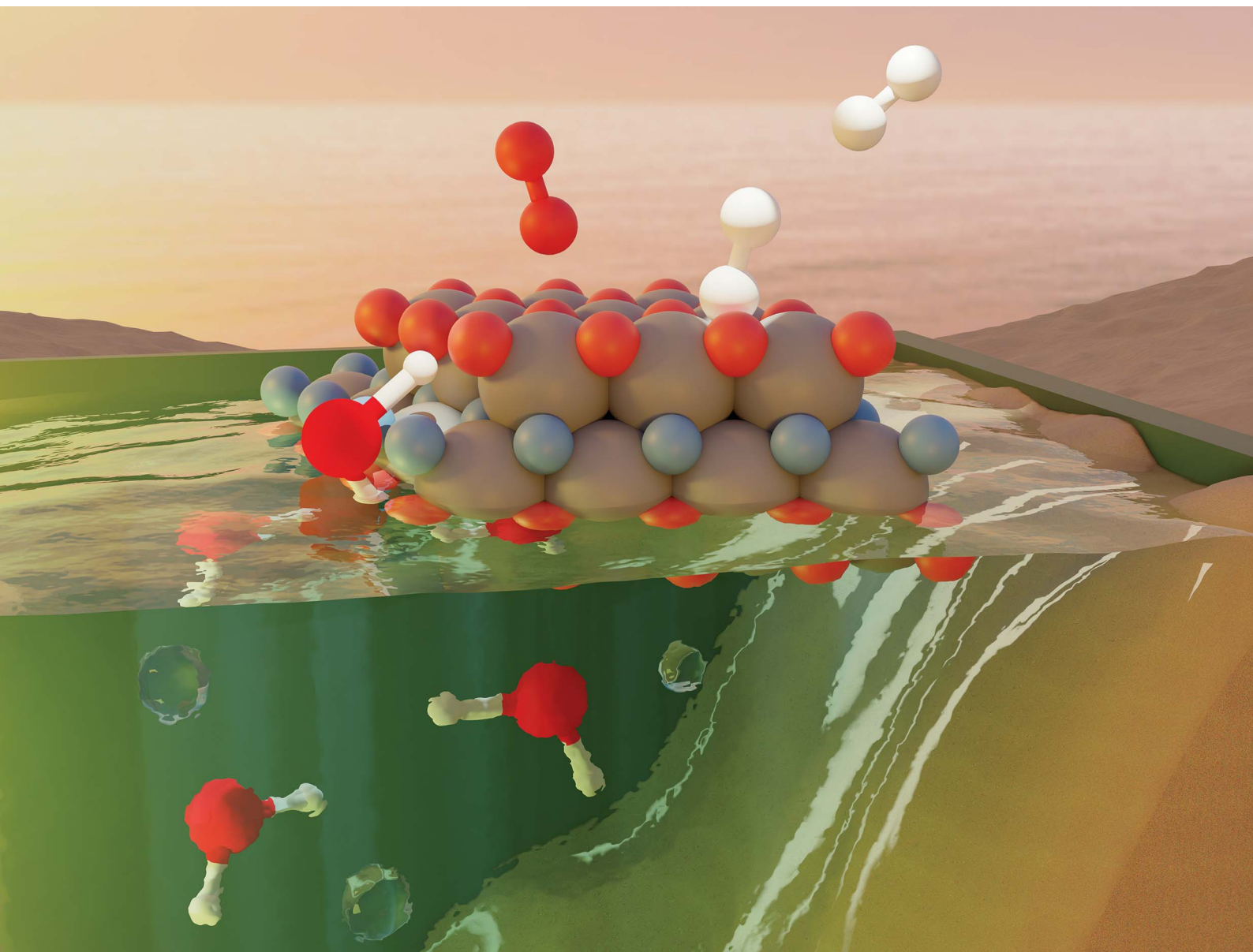
PAPER
Carmen Sousa *et al.*
Exploring the photoactive properties of promising MXenes
for water splitting

ROYAL SOCIETY
OF CHEMISTRY

Check for updates

Exploring the photoactive properties of promising MXenes for water splitting†

Diego Ontiveros, [iD] Francesc Viñes [iD] and Carmen Sousa [iD] *

The photoactive properties and effectiveness of a selected group of ten terminated MXenes—Sc_2CT_2, Y_2CT_2 (T = Cl, Br, S, and Se), Y_2Cl_2 and Zr_2CO_2—has been deeply studied by means of density functional theory (DFT). Here it is demonstrated that the studied MXenes exhibit robust energetic and dynamical stability, having all an indirect bandgap, while most of them with values within the visible spectrum, and also exhibiting suitable band alignment for the water splitting reaction. The charge density distribution of the valence band maximum (VBM) and conduction band minimum (CBM) is found to be separated across different layers with low overlaps, below 30%. Most MXenes present high charge carrier mobilities with favourable electron–hole disparities, with Sc_2CBr_2 also presenting directional charge carrier transport. Additionally, these materials show strong optical absorption ($\sim 10^5$ cm^{-1}) in the visible spectrum, translating to promising solar-to-hydrogen (STH) efficiency theoretical limits, up to 23%. Overall, the combination of all these features positions MXenes among the optimal materials for efficient photocatalytic water splitting.

1. Introduction

The continual rise in global energy consumption and concerns regarding environmental contamination make imperative to prioritize the development of renewable energy resources that are neither dependent on fossil fuels nor emit greenhouse gases.[1,2] Hydrogen (H_2), a carbon-zero-emission fuel, possessing high calorific value, high energy density, and excellent energy storage capacity, has the potential to significantly contribute at addressing the pressing sustainability and global warming challenges that mankind is currently facing.[3,4] The interest in H_2 production stems not only from its properties but also from its capability to be produced from renewable and abundant resources, such as water (H_2O). This occurs in the so-called water splitting process, where water is broken down into H_2 and oxygen (O_2) using a catalyst to facilitate the cleavage, given the high energy demand of the process. On the other hand, solar energy represents an inexhaustible, clean, and renewable energy source, and has attracted widespread attention, presenting itself as a viable option for driving the water splitting reaction, with materials acting as photocatalysts for the process.[5,6]

For a material to be photoactive in a specific reaction, it needs to be a semiconductor with a bandgap larger than the redox potential of the targeted reaction, which is 1.23 eV for water splitting. Ideally, this bandgap should fall within the visible light

spectrum so that sunlight could be effectively utilized in its most intense spectrum region. Additionally, the band edges of this bandgap—*i.e.* the valence band maximum (VBM) and conduction band minimum (CBM)—must be properly aligned, with the VBM positioned below the oxidation potential and the CBM above the reduction potential of the reaction.[7] In this context, the search for new materials that meet these conditions has been accelerated in the last years. One of the promising candidates for accomplishing the water splitting photocatalysis is the MXene family of materials. Being one of the most prominently emerging 2D nanomaterials in the last decade, MXenes have become a worldwide research hub due to their unique characteristics and wide application in many fields, including energy storage and electronics, where they excel in supercapacitors and batteries, as well as environmental applications such as water purification and CO_2 capture. MXenes are even making strides in biomedical applications, offering potential in areas like drug delivery, biosensing, and tissue engineering due to their biocompatibility and tuneable properties.[8–10] MXenes are a family of few-layered transition metal (TM) carbides and nitrides, with $M_{n+1}X_n$ chemical formula, where M is an early TM from groups III to VI—*i.e.* Sc, Y, Ti, Zr, Hf, V, Nb, Ta, Cr, Mo, and W—, X can be carbon or nitrogen, and $n = 1$–4.[9,11] Depending on their synthesis route, the chemical environment, and the physical conditions they are exposed to, MXenes can have their surface easily functionalized with a termination, T_x, updating the general chemical formula to $M_{n+1}X_nT_x$. The usual synthesis of MXenes involves selectively etching A elements from bulk layered MAX materials precursors, $M_{n+1}AX_n$, where A is typically a group XIII-XVI element.[12] The etching process is commonly carried out using a hydrofluoric

Departament de Ciència de Materials i Química Física & Institut de Química Teòrica i Computacional (IQTCUB), Universitat de Barcelona, c/ Martí i Franquès 1-11, 08028, Barcelona, Spain. E-mail: c.sousa@ub.edu

acid (HF) solution,[13] which produces terminations such as –O, –F, –OH, and –H.[14] Nevertheless, recent studies employing synthetic methods based on molten salts have reported new MXenes terminated with –S, –Se, –Te, –NH, –Cl, –Br, and –I, as well as pristine MXenes with no termination.[15,16]

Given this vastly wide compositional and structural variability, the experimental exploration of the MXene family as adequate photocatalysts can be an expensive and time-consuming task. For that reason, computational tools and methodologies aided at accelerating this process and gaining a deeper understanding of the photoactive nature of these materials.[17–20] Through high-throughput comprehensive computational screenings, more than 4000 MXenes structures have been previously evaluated for their photoactive properties, with a focus on bandgap and band alignment. This analysis identified ten promising MXenes for photocatalytic water splitting, exhibiting suitable bandgaps and band alignments.[19,20] Note that, while the bandgap size and alignment of the valence and conduction bands are necessary requirements for photocatalytic water splitting, as aforementioned, they alone do not account for the entirety of the process,[7] and other aspects, including optical absorption,[21] exciton formation and carrier mobility,[17] can bias the full process. In this work, we selected the ten most promising MXenes from the previously mentioned computational screenings, mainly Zr_2CO_2, Sc_2CT_2, Y_2CT_2 (T = –Cl, –Br, –S, and –Se), and Y_2CI_2, for further computational evaluation to assess their efficiency as photoactive catalysts. Particular MXenes with group III TMs have already garnered significant attention for their electronic and photoactive properties.[18,22,23] However, there remains a lack of studies exploring certain terminations, such as –Br or –I halides and –S or –Se chalcogenides. The present study addresses this

gap by also considering these less-explored terminations, while providing new insights into their potential for water splitting photocatalysis. The conducted electronic structure calculations, along with the analysis of optical absorption, solar-to-hydrogen efficiency, charge distribution, and carrier mobilities, reveal that the Zr_2CO_2 and group III halide-terminated MXenes demonstrate superior photocatalytic properties compared to their chalcogen-terminated counterparts. While our results demonstrate that the MXenes have suitable electronic structures and band alignments for photocatalytic water splitting, a comprehensive understanding of the hydrogen evolution reaction (HER) and oxygen evolution reaction (OER) mechanisms, with the corresponding Gibbs free energy profile—including active sites at terminations or edges, adsorption dynamics, and reaction pathways in the excited state—requires further investigation, likely involving the use of hybrid functionals and powerful computational resources. Such studies would complement our current findings and guiding the design of efficient MXene-based photocatalysts.

2. Computational details

2.1. Structural models

Pristine MXene structures, with $M_{n+1}X_n$ chemical formula, consist of M and X atom intercalated close-packed layers, with the number of layers depending on the n number. Two possible stackings emerge for such systems; ABC stacking, see Fig. 1a, with the M layers in two different relative positions, or ABA stacking, see Fig. 1b, with the M layers in the same relative position along the vacuum direction. The terminated MXenes, $M_{n+1}X_nT_x$, are initially built by adding the T_x atoms to the relaxed pristine MXene structures, sampling different surface
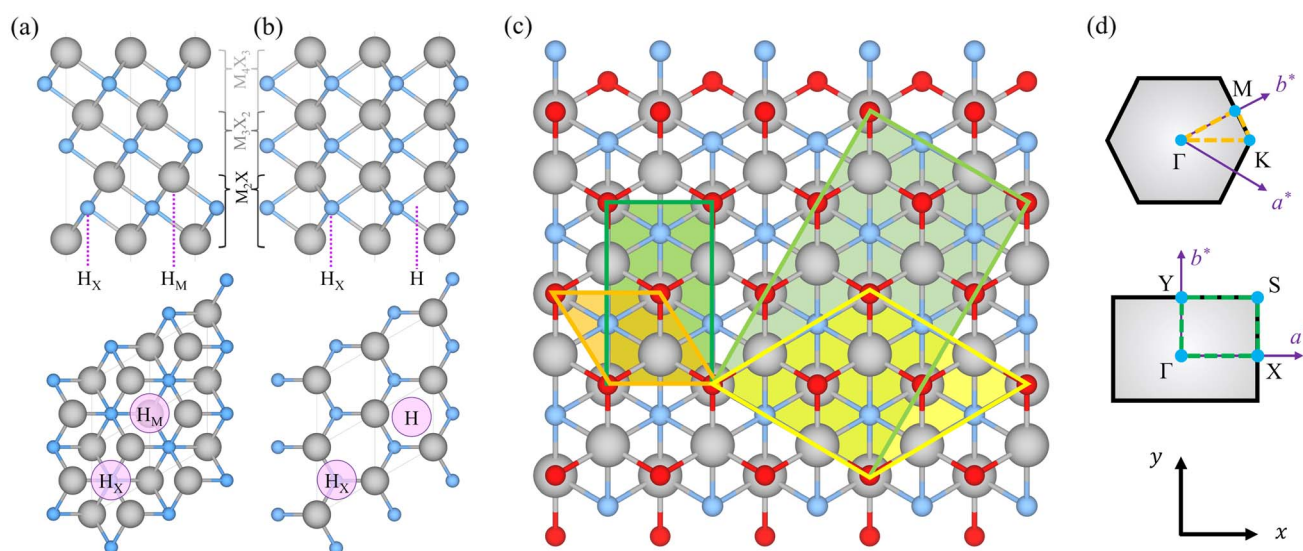
Fig. 1 MXene structures showing (a) ABC and (b) ABA stackings, with the lateral view on the upper panel and the top view on the bottom panel. The purple dotted lines in the lateral view and the purple circles on the surface mark the high symmetry sites explored for possible termination placement. Lines in gray indicate the unit cell. (c) Top view representation of a terminated MXene, with the $p(1 \times 1)$ hexagonal cells marked in orange and its correspondent orthogonal $c(1 \times 1)$ cell in green, while in yellow and light green corresponding larger $p(\sqrt{3} \times \sqrt{3})$ R30° and $c(3 \times 1)$ cells are represented as used for the distorted S- and Se-terminated structures. In all cases, gray, blue, and red spheres represent the M, X, and T atoms, respectively. (d) Reciprocal cell, high symmetry points, and explored **k**-paths for the hexagonal and orthonormal cells, respectively.

This journal is © The Royal Society of Chemistry 2025

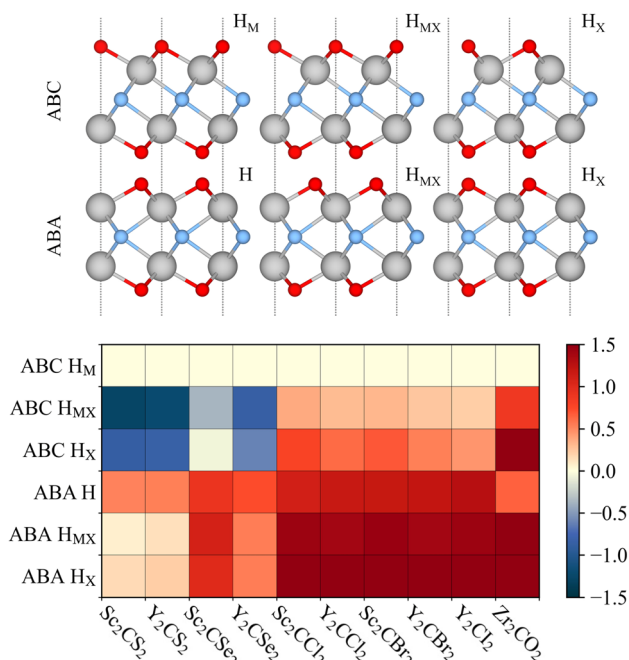*J. Mater. Chem. A*, 2025, **13**, 3302–3316 | **3303**

Fig. 2 Side view of the six possible terminated MXene structures (upper panel), using the same colour code as in Fig. 1. Relative energies, ΔE, in eV, with respect to the ABC H_M structure (bottom panel) for the possible terminated MXene geometries for the studied cases.

hollow sites, as indicated in Fig. 1. The explored sites are: the metal hollow in ABC stacking, H_M, located above an underlying metal atom, the simple hollow in ABA stacking, H, placed with no atoms underneath, the carbon or nitrogen hollows, H_X, with an underlying X atom for both stackings, and a mixture of H_M (H) and H_X on opposite MXene surfaces for ABC (ABA) stacking, H_{MX}. By combining stacking and hollow sites, each terminated MXene has six possible structures, see Fig. 2. This site notation will be used in the oncoming discussion.

These structures were modelled using a $p(1 \times 1)$ hexagonal unit cell, as in Fig. 1c. The slab models were represented with 30 Å of vacuum perpendicular to the MXene 2D surface, which previous studies and present tests revealed to be enough to avoid self-interaction,[24,25] and provided a good precision to the band alignment and vacuum energy calculations.[19] The structures investigated in this study are derived from a selection of 10 promising MXenes identified through previous high-throughput computational screening aimed at assessing MXenes for photocatalytic water splitting.[19,20] These include Sc_2CT_2, Y_2CT_2 (T = −Cl, −Br, −S, and −Se), Y_2CI_2 and Zr_2CO_2, which already exhibit an adequate band alignment, and our subsequent investigation aims to delve deeper into their photoactive effectiveness in the water splitting process.

2.2. Methods

The electronic structure of the considered MXenes has been studied in the framework of density functional theory (DFT).[26,27] Calculations were carried out using the Vienna *ab initio* simulation package (VASP),[28] employing the Perdew–Burke–

Ernzerhof (PBE)[29] exchange–correlation functional within the generalized gradient approximation (GGA).[30] Additionally, to achieve a more reliable estimation of the bandgap and electronic structure, further calculations were performed using the PBE0 hybrid functional, including a 25% of non-local Fock exchange.[31,32] During the calculations, atomic core electrons and their interaction with valence electrons were represented using projector augmented wave (PAW) pseudopotentials,[33] while the valence electrons were described using a planewave basis set with an optimal kinetic energy cutoff of 415 eV, considering spin-polarization. The geometry optimizations were considered converged when the forces acting on the nuclei were all below 0.01 eV Å^{-1} and a 10^{-6} eV threshold was chosen as the electronic convergence criterion. All atomic positions and cell parameters were allowed to relax during the optimizations. Optimal Γ-centred $7 \times 7 \times 1$ Monkhorst–Pack[34] **k**-points grids were employed for the Brillouin zone integration.

The PBE0 bandstructure calculations using planewaves require high computational resources, and so, such calculations were carried out using the Fritz-Haber Institute *ab initio* materials simulation (FHI-AIMS) package,[35] an all-electron program that uses numerical atomic orbitals (NAOs) as basis set. The self-consistent field and optimization criteria for FHI-AIMS are set equivalent to the ones used in VASP, to maintain the same computational playground, and a light Tier-1 level was used as the basis set. The bandstructure was explored along the $\Gamma \rightarrow K \rightarrow M \rightarrow \Gamma$ path, see Fig. 1d.

To assess the dynamical stability of MXenes, the phonon spectra were calculated using PHONOPY,[36] based on the force constants computed by density functional perturbational theory within VASP (VASP-DFPT),[37] using a $4 \times 4 \times 1$ supercell and a reduced $3 \times 3 \times 1$ **k**-points grid. From each phonon spectrum, the artificial mode corresponding to the vertical translation of the slab was disregarded from the analysis.

2.3. Photocatalytic properties

To further evaluate the photoactive qualities and effectiveness of the selected MXenes, a set of properties have been computed as check-points to be fulfilled.[7] Firstly, for a material to be photoactive in a given photoelectrocatalytic reaction, its band edges—*i.e.* the valence band maximum (VBM) and conduction band minimum (CBM)—must suitably align with respect the half-reaction potentials of the redox reaction, with the VBM and CBM being below or exceeding the oxidation and reduction potentials, respectively. In the context of photocatalytic water splitting, the reduction (H$^+$/H$_2$) and oxidation (H$_2$O/O$_2$) absolute potentials are −4.44 eV and −5.67 eV, respectively.[38] The band alignment is calculated from the Fermi level, E_F, and the bandgap, E_g:

$$E_{VBM} = E_F - V_v \quad E_{CBM} = E_{VBM} + E_g \tag{1}$$

where V_v is the electrostatic potential in the vacuum region of the slab model, extracted from the local potential plot along the vacuum direction—perpendicular to the MXene surface. In the case of S- and Se-terminated MXenes with H_{MX} structures, the asymmetry between both exposed surfaces renders them as

3304 | *J. Mater. Chem. A*, 2025, **13**, 3302–3316

This journal is © The Royal Society of Chemistry 2025

Janus materials, and dipole corrections were applied along the vacuum direction to account for their intrinsic electric field (IEF).

An ideal photocatalyst would present a low exciton recombination rate, which can be fostered by a good separation between the created charge carriers. This can be estimated by calculating the electron and hole effective masses, m^*, and charge carrier mobility, μ. When the electron, μ_e, and hole, μ_h, mobilities are significantly different, it is an indication that one charge carrier type is dispersing more rapidly than the other, potentially resulting in their spatial separation throughout the material, and eventually enhancing the overall efficiency of the charge carrier dynamics. Additionally, the directionality of the charge carriers can also influence their separation. The effective mass can be estimated as:

$$m^* = \hbar^2 \left(\frac{\partial^2 E(\mathbf{k})}{\partial \mathbf{k}^2} \right)^{-1} \tag{2}$$

where $\hbar$ is the reduced Plank's constant, and $E(\mathbf{k})$ is the band energy at the reciprocal point $\mathbf{k}$, where $\mathbf{k}$ are generally estimated along high symmetry band paths. Thus, m^* can be computed by assuming a parabolic dispersion around the VBM and CBM as:

$$E(\mathbf{k}) = \frac{\hbar^2 |\mathbf{k}|^2}{2m^*} \tag{3}$$

fitting it to a second order polynomial. The charge carrier mobility can be derived from deformation potential theory (DPT),[39] as:

$$\mu_i = \frac{e\hbar^3 C_{2D,i}}{k_B T m_i^* \overline{m} E_{d,i}^2} \tag{4}$$

where e, k_B, and T are the electron charge, Boltzmann's constant, and temperature, respectively. m_i^* is the carrier effective mass along the direction of motion i and $\overline{m} = \sqrt{m_x^* m_y^*}$ represents the geometric average of effective masses along x- and y-directions. $C_{2D,i} = [\partial^2 E_T / \partial \delta^2]/S_o$ is the elastic modulus under uniaxial strain along a given i direction, with E_T being the total energy of the system, δ the uniaxial strain along the transport direction, and S_o the area of the equilibrium unit cell. Finally, $E_{d,i}$ designates the deformation potential constant of holes and electrons in the VBM and CBM, respectively, along the transport direction, and is defined as $\partial E_{edge}/\partial \delta$, where E_{edge} is the VBM or CBM energy. Both $C_{2D,i}$ and $E_{d,i}$ can be estimated by parabolic and linear fitting of the variables involved, respectively. For the charge carrier mobility calculations, an orthogonal unit cell was used, see Fig. 1c, which facilitates the selection of two perpendicular directions. In MXenes, these directions are typically referred to as *zigzag* and *armchair* directions, which in our chosen unit cell, correspond to the x and y axes, respectively.

In the quest for a low exciton recombination, another property to consider is the charge density separation between the VBM and CBM. In this work, to give a quantitative numerical estimation of this spatial separation, we computed the overlap integral between both densities:

$$S_{ab} = \int \rho_a \rho_b \mathrm{d}V \quad \hat{S}_{ab} = \frac{S_{ab}}{\sqrt{S_{aa} S_{bb}}} \tag{5}$$

where ρ is the charge density of the VBM or CBM, V is the volume, and $\hat{S}_{ab}$ is the normalized overlap integral.

An optimal condition to use sunlight as an energy vector for the photocatalytic reaction is a bandgap within the visible range (1.8–3.1 eV), but, in order to fully harvest this sunlight, another key component is the absorption of light in the visible spectrum. This is studied here by means of the frequency-dependent dielectric function, $\varepsilon(\omega)$, defined as:

$$\varepsilon(\omega) = \varepsilon_r(\omega) + i\varepsilon_i(\omega) \tag{6}$$

where ε_r and ε_i are its real and imaginary parts, respectively, which can be used to derive the absorption coefficient, $\alpha(\omega)$:

$$\alpha(\omega) = \frac{\sqrt{2}\omega}{c} \left[\sqrt{\varepsilon_r^2(\omega) + \varepsilon_i^2(\omega)} - \varepsilon_r(\omega) \right]^{1/2} \tag{7}$$

where c is the speed of light. To compute the dielectric function and the optical absorption spectra, the many body perturbation Green's function and screened coulombic interaction (GW)[40] Bethe–Salpeter equation (BSE)[41] GW-BSE approach is used, which allows to computing accurate absorption spectra, including electron–electron and electron–hole interactions. These methods vastly depend on the used parameters, and, in the present case, an optimal planewave energy cutoff of 200 eV was found, together with 960 bands for the GW calculations, while 8 occupied and 16 unoccupied bands were selected to describe the excitons in the BSE calculations. All the calculations were performed using converged 13 × 13 × 1 Monkhorst–Pack $\mathbf{k}$-point grids, except for the distorted MXenes, *vide infra*, for which a 5 × 5 × 1 grid was chosen due to the high computational cost associated with the necessary larger unit cell and increased number of atoms. From the BSE optical spectra, the optical gap, E_{opt}, can be extracted. This value, along with the minimum direct electronic bandgap, $E_g^{PBE0,D}$, can be used to compute the exciton binding energy, $E_b = E_g^{PBE0,D} - E_{opt}^{opt}$.[21,42]

The solar-to-hydrogen (STH) efficiency has been also estimated. This is a key parameter for evaluating the efficiency of converting solar light into hydrogen fuel. In here one computes the upper limit of the STH, as based on a previous work,[43] assuming 100% efficiency of the catalytic reactions. The STH can be decomposed into light absorption, η_{abs}, and carrier utilization, η_{cu}, efficiencies, which take the form of the following equations:

$$\eta_{abs} = \frac{\int_{E_{opt}}^{\infty} P(\omega) \mathrm{d}\omega}{\int_0^{\infty} P(\omega) \mathrm{d}\omega} \tag{8}$$

$$\eta_{cu} = \Delta G \frac{\int_E^{\infty} \frac{P(\omega)}{\omega} \mathrm{d}\omega}{\int_{E_{opt}}^{\infty} P(\omega) \mathrm{d}\omega} \tag{9}$$

where $P(\omega)$ is the air mass at 1.5 atm thickness global (AM1.5G) solar energy flux at photon energy,[44] ΔG is the water redox potential difference of 1.23 eV, and E is the photon energy that can be actually utilized for water splitting. Considering the

This journal is © The Royal Society of Chemistry 2025

J. Mater. Chem. A, 2025, **13**, 3302–3316 | **3305**

existing barriers for HER and OER, extra energy is demanded to overcome those barriers, which should be added in E. According to the previous reports, considering the overpotentials of OER and HER co-catalysts and the energy loss during carriers migration between materials, suitable overpotentials of 0.2 and 0.6 V are assumed for HER and OER, respectively.[43,45,46] Thus, the E value of can be expressed as:

$$E = \begin{cases} E_{opt} & \text{if } \chi_{H_2} \geq 0.2 \text{ and } \chi_{O_2} \geq 0.6 \\ E_{opt} + 0.2 - \chi_{H_2} & \text{if } \chi_{H_2} < 0.2 \text{ and } \chi_{O_2} \geq 0.6 \\ E_{opt} + 0.6 - \chi_{O_2} & \text{if } \chi_{H_2} \geq 0.2 \text{ and } \chi_{O_2} < 0.6 \\ E_{opt} + 0.8 - \chi_{H_2} - \chi_{O_2} & \text{if } \chi_{H_2} < 0.2 \text{ and } \chi_{O_2} < 0.6 \end{cases} \quad (10)$$

where χ_{H_2} and χ_{O_2} are the overpotentials for HER and OER, respectively, computed as the difference between the band edge (VBM or CBM) and the correspondent redox half reaction potential. With both these contributions, the STH efficiency is defined as:

$$\eta_{STH} = \eta_{abs} \cdot \eta_{cu} \quad (11)$$

For Janus structures, with a difference between vacuum levels of the two surfaces, $\Delta\phi$, like for S- and Se-terminated MXenes, the intrinsic electric field does positive work for the separation of photon excited electrons and holes during the processing of photocatalytic water splitting, and therefore it should be added into the total energy. Hence, the corrected STH efficiency of photocatalytic water splitting for 2D materials with intrinsic electric field, η'_{STH}, is defined as:

$$\eta'_{STH} = \eta_{STH} \frac{\int_0^\infty P(\omega)d\omega}{\int_0^\infty P(\omega)d\omega + \Delta\phi \int_{E_{opt}}^\infty \frac{P(\omega)}{\omega}d\omega} \quad (12)$$

3. Results and discussion

3.1. Structure stability

To assess the most stable structure from the six possible ones for each studied MXene, the relative energy of the different conformations is computed with respect to the ABC H_M structure. The results, presented in Fig. 2, show how all systems prefer the ABC stacking with the termination in the metal hollows, H_M, except from S- and Se-terminated MXenes, for which the H_{MX} termination arrangement is more stable, consistent with other theoretical studies.[47] The forthcoming discussion and results will be based on these most stable structures.

Concerning the group III S-terminated MXenes, previous theoretical studies reported the existence of a slightly more stable distorted phase.[48,49] In an attempt to confirm these findings, we optimized these systems applying a $p(\sqrt{3} \times \sqrt{3})$ R30° larger unit cell, as depicted in Fig. 1c, to allow for symmetry breaking. After introducing an initially random distortion and re-optimizing the system, we observed that for S- and Se-terminated cases, the structure with the minimum energy indeed corresponded to a distorted phase, as shown in
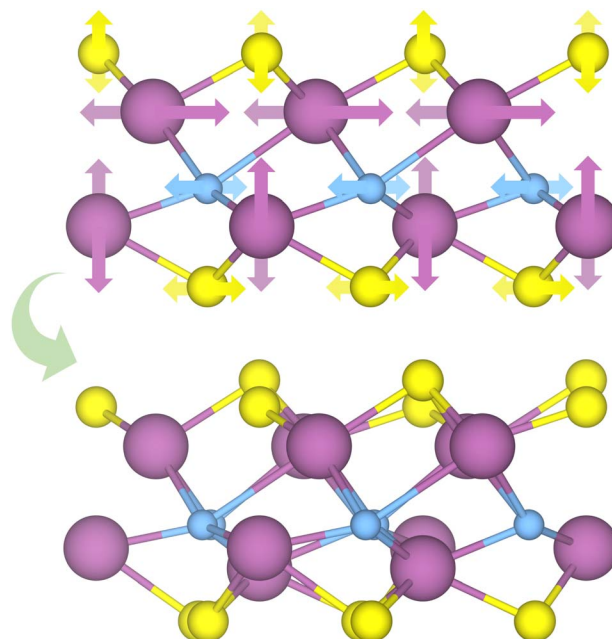

Fig. 3 Schematic representation of the distortion movement from the regular H_{MX} structures to the new distorted phases. The darker and lighter arrows mark the front or back atoms, respectively.

Fig. 3, in accordance with the mentioned literature. However, the differences in energy per MXene unit between the regular and distorted phases were found to be almost negligible in all cases, similar to findings by Zhu et al.,[47] with deviations of approximately −0.03 eV and −0.02 eV for distortions in Sc_2CS_2 and Sc_2CSe_2, respectively, and at most −0.13 eV for both Y_2CS_2 and Y_2CSe_2 MXenes, thus well within the standard DFT accuracy. Therefore, while these distorted phases will still be discussed in the following, the primary focus will remain on the regular structures, as one can safely regard these as competitive domains.

Table 1 gathers the lattice parameter, a, and width, d, for all studied MXenes, including the distorted ones, marked with a d-prefix on their names. The computed values are in good agreement with other computational estimates,[47,50,51] and also with experimentally synthesised systems similar to those here studied, like stacked Sc_2CCl_2 MXene sheets.[52] The Zr_2CO_2 MXene presents the lowest lattice parameter among the studied cases, and within the group III MXenes, Y-MXenes have slightly larger cell parameters compared to their Sc counterparts, owing to the larger atomic radius of Y. Halide-terminated MXenes display significantly larger widths than chalcogen-terminated ones, exceeding them by more than 1 Å on average, with Y_2CI_2 exhibiting the largest thickness. Additionally, it is observed that the distortion found on the chalcogen-terminated MXenes leads to a slight increase in MXene width compared to the regular structures.

To evaluate the thermodynamical stability of the studied MXenes, we calculated the cohesive, E_{coh}, and formation, E_{form}, energies, see Table 1, and compared them to similar 2D materials that have been shown to be stable. Both E_{coh} and E_{form} energies can be extracted from the following expressions:

3306 | J. Mater. Chem. A, 2025, **13**, 3302–3316

This journal is © The Royal Society of Chemistry 2025

Table 1 Structural and energetic properties of the studied MXenes, where a and d represent the lattice parameter and width, in Å, respectively, and E_{coh} and E_{form}, represent the cohesive and formation energies, in eV, respectively as defined in eqn (13) and (14), respectively. The MXene cases preceded by the d-prefix indicate a structural distorted phase

MXene	a (Å)	d (Å)	E_{coh} (eV)	E_{form} (eV)
Zr_2CO_2	3.30	4.70	−7.68	−10.97
Sc_2CS_2	3.77	4.67	−5.52	−4.97
Y_2CS_2	4.09	4.82	−5.52	−4.87
Sc_2CSe_2	3.84	4.98	−5.16	−4.21
Y_2CSe_2	4.15	5.19	−5.17	−4.16
Sc_2CCl_2	3.45	5.81	−5.41	−7.84
Y_2CCl_2	3.72	6.20	−5.42	−7.77
Sc_2CBr_2	3.52	6.12	−5.09	−6.74
Y_2CBr_2	3.77	6.55	−5.13	−6.84
Y_2CI_2	3.88	6.97	−4.77	−5.32
d-Sc_2CS_2	6.55	4.80	−5.52	−5.00
d-Y_2CS_2	7.09	5.03	−5.54	−4.99
d-Sc_2CSe_2	6.66	5.14	−5.16	−4.23
d-Y_2CSe_2	7.18	5.41	−5.19	−4.29

$$E_{coh} = \frac{E_{M_2CT_2} - (2E_M + E_C + 2E_T)}{5} \qquad (13)$$

$$E_{form} = E_{M_2CT_2} - (2E(M) + E(C) + 2E(T)) \qquad (14)$$

where $E_{M_2CT_2}$ is the total energy for the terminated MXene, E_i (i = M, C, or T) are the energies of an isolated i atom in vacuum, and $E(i)$ are the energies per atom for the most stable structure of i element in normal conditions (*e.g.*, graphite for C, hcp bulk structures for the transition metals, *etc.*). In terms of cohesive energies per atom, the group III-based MXenes exhibit very similar values, ranging from −4.5 to −5.5 eV per atom.

These values are sensibly smaller than that of graphene (−7.97 eV per atom)[53] but surpass those of the already-synthesized silicene (−4.57 eV per atom),[54] phosphorene (−3.59 eV per atom),[55] and other 2D materials.[56] Notably, the Zr_2CO_2 MXene presents a cohesive energy comparable to graphene, indicating its strong bonding and stability.

The formation energies show similar patterns, with the Zr_2CO_2 MXene standing out among the others. Here, halide-terminated MXenes exhibit more negative formation energies than chalcogen-terminated ones, suggesting that the former are thermodynamically more stable than the latter with respect to their reference materials. For the distorted structures of chalcogen-terminated MXenes, the formation and cohesive energies remain very similar to those of their regular structures, as the distortion does not result in a significant gain in stability. Overall, the large negative values in the formation and cohesive energies indicate the structural stability and strong bonding formation of these MXene structures.

To further investigate their plausible viability, the dynamical stability of the resulting optimal MXenes was put under scrutiny, and their phonon spectra were estimated. Fig. 4 presents the results for the regular structures while the distorted phases are displayed in Fig. S1 of the ESI.† None of the phonon modes display significant negative frequencies, suggesting the overall stability of the materials. This finding aligns with phonon calculations reported in other references for MXene systems.[17,18,57] Note that while small imaginary frequencies below 30 cm^{-1} near the Γ point were observed for S- and Se-terminated MXenes, these can be safely attributed to numerical noise due to the vacuum region or the employed **k**-point mesh.[58–60] While the previous phonon spectrum calculations confirmed the dynamical stability of the studied MXenes in their ground state, it is crucial to also assess their stability in
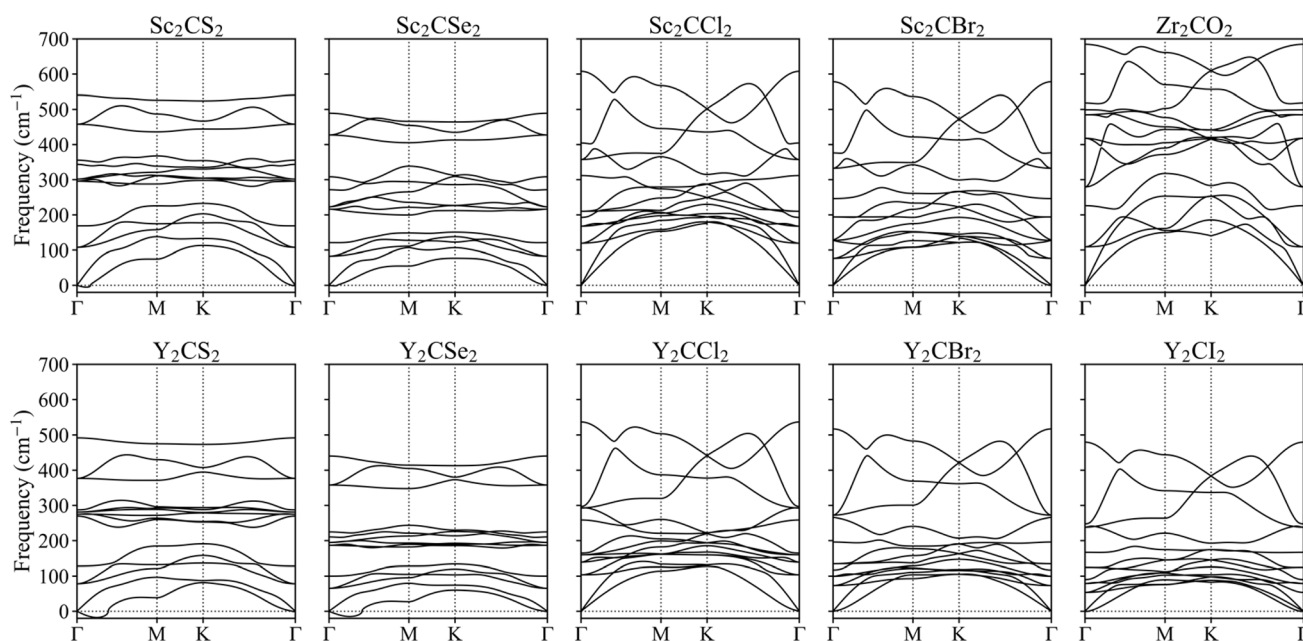
Fig. 4 Phonons spectra along the $\Gamma \rightarrow K \rightarrow M \rightarrow \Gamma$ k-points paths for the studied MXenes, using a regular $p(1 \times 1)$ unit cell.

This journal is © The Royal Society of Chemistry 2025

J. Mater. Chem. A, 2025, **13**, 3302–3316 | **3307**

excited states to better understand their behaviour under photocatalytic conditions. To this end, we selected the Zr_2CO_2 MXene for further investigation and performed phonon calculations in the excited triplet state. The phonon spectra exhibited all positive frequencies, see Fig. S2 of the ESI,† indicating that Zr_2CO_2 remains dynamically stable when photoexcited.

Although this study focuses on the intrinsic photocatalytic properties of MXenes, it is well-documented that light irradiation can induce surface defects or generate new electronic states in MXenes, which may influence their stability and photocatalytic efficiency. For example, it has been observed that oxygen vacancies or other point defects can form on MXene surfaces,[61] potentially altering electronic states and band alignment. Similarly, corrosion or degradation of the material may occur under certain conditions or environments.[62] Additionally, the generation of mid-gap states due to surface defects could impact on charge separation and recombination processes.[63] Thus, further research is required to investigate these effects under more realistic photocatalytic conditions.

3.2. Electronic structure

The electronic properties of MXenes were investigated through bandstructure and density of states (DOS) calculations. Since the PBE exchange–correlation functional, as many other low-rung functionals, are known to systematically underestimate the bandgap energies,[32] as happen with the here explored MXenes, see Table 2, the electronic structure calculations were conducted using the PBE0 hybrid functional, known to deliver estimates comparable to reference GW while being computationally more affordable.[20] The bandstructure and DOS for each MXene case is presented in Fig. 5, while for the four distorted MXene structures the results are found on Fig. S3 of the ESI.† All the selected promising cases exhibit a bandgap larger than 1.23 eV, which is necessary for photocatalysing the water splitting process. Most of these systems have a bandgap within the

visible region, while the chalcogen-terminated MXenes show bandgap values that are slightly shifted towards the UV region. For the distorted structure MXene cases, the electronic structure remains very similar, with bandgap values also being comparable, although slightly reduced, likely due to the creation of new electronic states when the symmetry is broken. These new states appear just above the VBM and below the CBM, leading to a minor decrease in the overall bandgap.

When inspecting the bandstructures, it can be seen how the bandgap normally goes from the VB $\mathbf{\Gamma}$ to the CB $\mathbf{M}$ point, whereas in regular S-terminated MXenes, the bandgap implies the VB $\mathbf{\Gamma}$ point to (or close to) the CB $\mathbf{K}$ point. This last aspect is amended in the distorted structures, where all MXenes systematically present also a $\mathbf{\Gamma} \rightarrow \mathbf{M}$ transition. This feature underscores the indirect nature of the bandgap. The impact of an indirect bandgap on photocatalytic efficiency involves a balance between light absorption and charge carrier dynamics. While direct bandgaps typically enable stronger light absorption, indirect bandgaps can result in lower recombination rates, leading to longer carrier lifetimes. This extended lifetime enhances charge separation and improves the overall efficiency of photocatalytic processes. Such characteristics make indirect bandgaps advantageous in cases where carrier longevity is crucial for the desired reactions.[64,65]

Thanks to the atomic projections of the bandstructures and DOS, one can also discern how the VB and CB are distributed. The first bands of the VB mainly have contributions from the C and TM layers, sometimes separated by a gap from the lower energy bands, which are primarily contributed by the termination atoms. On the other hand, the CB is dominated by the d orbitals of the TM.
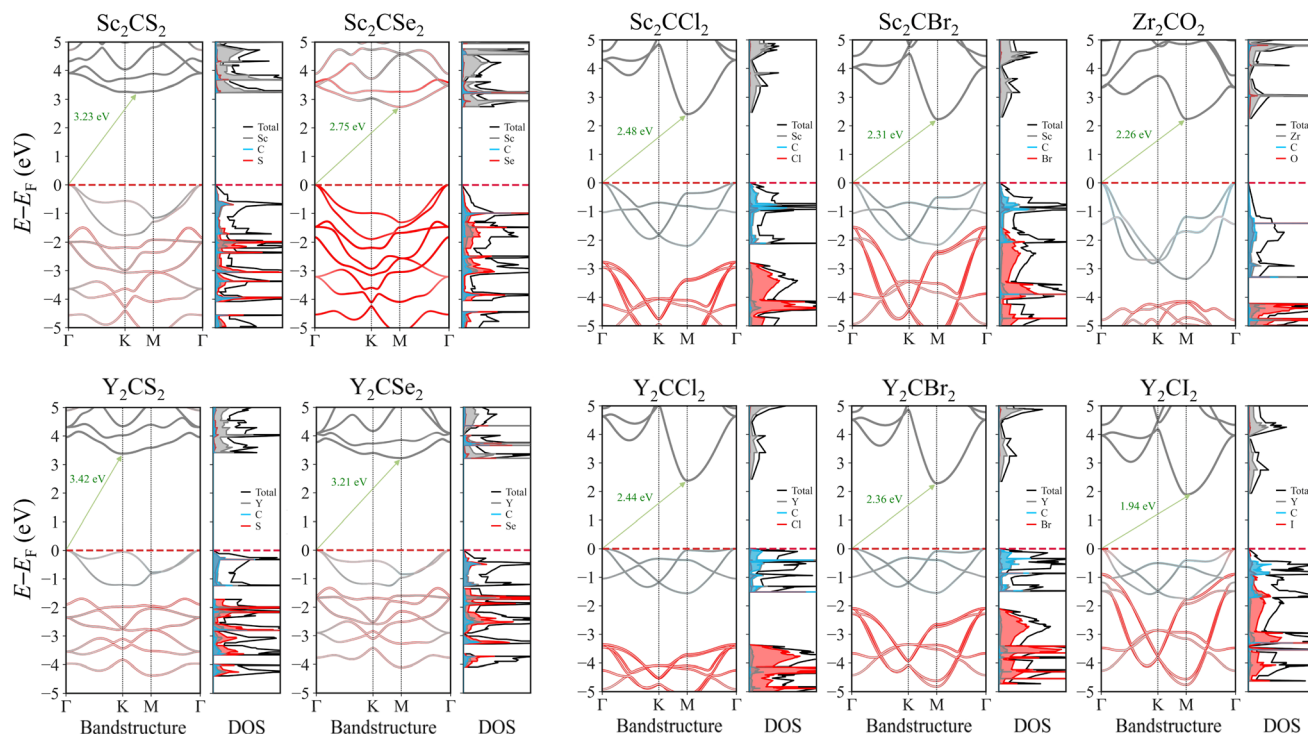
3.3. Band alignment

As above-mentioned, one crucial requirement for a suitable photocatalyst for the water splitting reaction is an adequate band alignment of the band edges with respect to the reaction oxidation/reduction potentials. In other words, the VBM location in the energy spectrum needs to be lower than the oxidation potential of H_2O/O_2, and the CBM position must exceed the reduction potential of H^+/H_2. These conditions are easily met by the studied candidates, see Fig. 6. Considering that S- and Se-terminated MXenes exhibit an H_{MX}-type structure, each exposed surface is topologically different, with different chemical environments. This variation between surfaces renders them as Janus materials. As a result, the electrostatic potential in the vacuum region on each side of the slab differs, generating an intrinsic electric field.[66] An example of this phenomenon is illustrated in Fig. 7, with $\Delta\phi$ representing the difference between the vacuum energies on each surface. For such MXenes with the termination on H_{MX} positions, the electrostatic potential of the surface in which the chalcogen is adsorbed on the H_X site is lower than when it is located on the H_M site, generating an intrinsic electric field from the H_X towards the H_M terminated surface. The previous has also an effect on the band alignment, since each surface will have its own band edge positioning. In Fig. 6b the band alignment of each surface is

Table 2 Bandgap properties for the MXene compound, where E_g^{PBE} and E_g^{PBE0} indicate the PBE and PBE0 indirect bandgaps, respectively, $E_{g,D}^{PBE0}$ marks the minimum energy direct bandgap, E_{opt} is the optical gap, with E_b being the exciton binding energy, all of them in given eV. The $\hat{S}_{ab}$ indicates the spatial overlap between the VBM and CBM, given in percentage

MXene	E_g^{PBE}	E_g^{PBE0}	$E_{g,D}^{PBE0}$	E_{opt}	E_b	$\hat{S}_{ab}$ (%)
Zr_2CO_2	0.87	2.26	3.34	2.87	0.47	27.92
Sc_2CS_2	1.58	3.23	3.83	3.34	0.49	35.22
Y_2CS_2	1.84	3.42	3.43	2.93	0.50	38.56
Sc_2CSe_2	1.21	2.75	3.48	3.15	0.33	31.92
Y_2CSe_2	1.70	3.21	3.73	2.99	0.74	34.59
Sc_2CCl_2	0.95	2.48	2.77	2.30	0.47	26.26
Y_2CCl_2	1.01	2.44	2.43	1.89	0.54	31.72
Sc_2CBr_2	0.79	2.31	2.74	2.31	0.44	27.19
Y_2CBr_2	0.94	2.36	2.37	1.85	0.52	30.75
Y_2CI_2	0.59	1.94	2.35	1.79	0.56	25.26
d-Sc_2CS_2	1.39	3.01	3.22	2.93	0.29	19.11
d-Y_2CS_2	1.67	3.20	3.37	2.65	0.72	27.72
d-Sc_2CSe_2	1.05	2.56	2.96	2.54	0.42	30.54
d-Y_2CSe_2	1.45	2.94	3.32	2.65	0.67	27.09

3308 | *J. Mater. Chem. A*, 2025, **13**, 3302–3316

This journal is © The Royal Society of Chemistry 2025

Fig. 5 PBE0 band structures and DOS for the studied MXenes, both projected onto the different atomic contributions. In grey, blue, and red are marked the TM, C, and T contributions, while black denotes the total sum. The green arrow marks the bandgap, with its correspondent value, in eV. The energies, given in eV, are referenced to the Fermi level, E_F, here placed at the VBM.
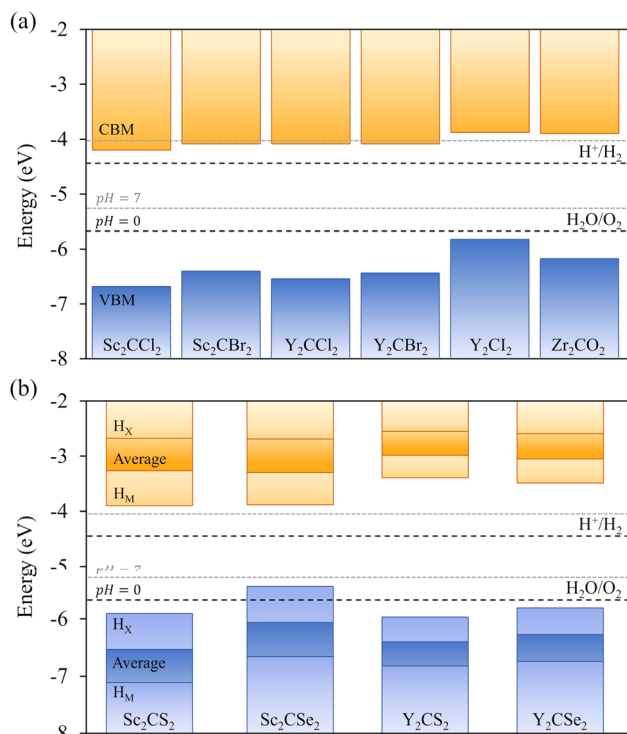
Fig. 6 Band alignment diagrams with respect to the H^+/H_2 and H_2O/O_2 redox potential energy levels, represented by the dotted lines, for (a) symmetric H_M (b) Janus H_{MX} MXene structures. The blue and orange bars indicate the VB and CB, respectively. For the Janus chalcogen-terminated MXenes (lower diagram), the band edge position is represented for each surface, and an average between them.

displayed for the H_{MX} Janus-like cases. Note that in thin 2D materials, the effect of the intrinsic field may not be crucial, yet here the average band alignment between both faces is provided, as if dipole corrections were not considered and the electrostatic potential was averaged in the vacuum level.
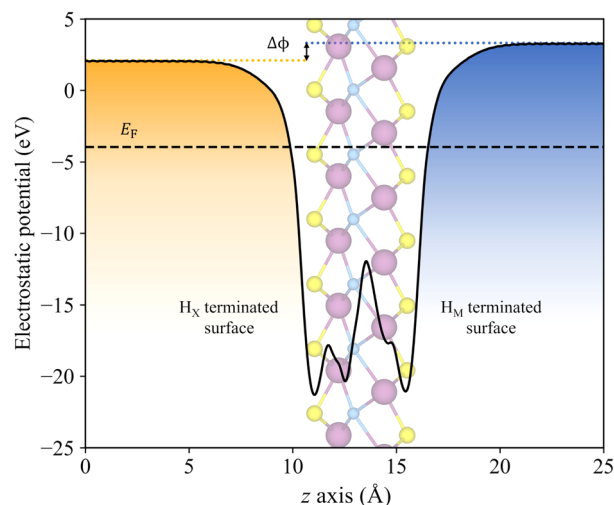
Fig. 7 Plane averaged electrostatic potential, in eV, along the z axis, in Å, for the Janus Sc_2CS_2 MXene. $\Delta\phi$ marks the difference between the vacuum potentials at each surface, indicated by the orange and blue dotted lines. The dashed black lines indicate the Fermi level. The orange and blue colours refer to main reaction each surface will carry out, HER for H_X terminated surface (orange section), and OER for H_M terminated surface (blue section).

This journal is © The Royal Society of Chemistry 2025

J. Mater. Chem. A, 2025, **13**, 3302–3316 | **3309**

Another important factor to consider is the pH, since the redox potentials are affected by pH conditions ($-5.67 + 0.059\cdot$pH eV for the oxidation and $-4.44 + 0.059\cdot$pH eV for the reduction). Usually, these potentials are given at standard conditions of pH = 0, and so, at very strong acidic conditions, indicated by the black dashed lines in Fig. 6, but here one should also consider a neutral case when pH = 7, marked by the grey dashed lines. In all cases, including the symmetric H_M structures and both faces of the Janus H_{MX} geometries, there is suitable band alignment for the overall water splitting reaction at pH = 0, with the sole exception of the Sc_2CSe_2 H_X face, which only fulfils the H^+/H_2 reduction potential alignment. Note that the intrinsic electric field present in these S- and Se-terminated MXenes facilitates the spatial separation of photoexcited electrons and holes. Given that the electric field direction goes from the H_X to the H_M terminated surface, electrons accumulate on the H_X face, and holes on the H_M face. This distribution helps separating the oxidation and reduction photocatalytic processes onto the faces, and in the case of Sc_2CSe_2, the H_X face, which is only capable of photocatalysing the HER process, will be enhanced by the accumulation of holes in that region.

When increasing the pH to 7, this just mentioned feature disappears, and the Sc_2CSe_2 MXene becomes capable of photocatalysing the overall process, as the other chalcogen-terminated MXenes do for the entire 0–7 pH range. However, this is not the case for some halide-terminated MXenes. When the pH is increased to 7, the Sc and Y cases terminated in –Cl and –Br lose, although by little, their ability to photocatalyze the HER process since the CBM barely falls below the reduction potential, although they would be capable of so at slightly acidic conditions. This highlights the ability to modulate which reaction occurs or is triggered based on the pH conditions, which can be convenient in the actual photocatalytic process setup.

For the distorted MXenes, see Fig. S4 of the ESI,† the band alignments correspond well with their respective regular structures, with the Sc_2CSe_2 H_X face still presenting suitable

band alignment only for the HER process at pH = 0. When increasing to pH = 7, similar conclusions can be withdrawn as in the non-distorted cases, since they still maintain the overall water splitting capabilities. However, in the distorted structure of Sc_2CSe_2, the CBM of the H_M face significantly decreases its energy, falling slightly below the reduction potential, reducing the efficiency on the HER photocatalysis, yet still maintaining suitable band alignment for OER.

3.4. Charge density

Efficient photocatalysts typically exhibit significant charge density separation between the VBM and CBM, which facilitates the effective separation and migration of photogenerated electron–hole pairs, thereby reducing recombination rates. Here, the VBM and CBM charge densities were gained for the investigated cases, encompassed in Fig. S5 of the ESI.† The halide-terminated MXenes and Zr_2CO_2 present the VBM distributed along the p orbitals of the C atoms, with minor contributions from the p orbitals of the terminations, while the CBM is centred around the TM layers, as seen in the example of Sc_2CCl_2 in Fig. 8a, in line with the orbital distribution observed in the projected DOS of Fig. 5. For the chalcogen-terminated MXenes, the asymmetry between the surfaces is also reflected in the charge density distribution. The VBM is more concentrated around the H_X face, predominantly around the C and T_x atoms, while the CBM is more centrally located, with major contributions from the TM and C layers.

Aside from providing a qualitative interpretation of the charge densities, a quantitative approach is tackled by computing the spatial overlap integral between the VBM and CBM charge densities, see Fig. 8b, with values listed in Table 2. This metric estimates the percentage of overlap between the charge densities at both band edges. The lowest overlaps are observed for Zr_2CO_2, Sc_2CBr_2, Sc_2CCl_2, and Y_2CI_2, in descending order, with all showing an overlap of less than 28%. The remaining MXenes
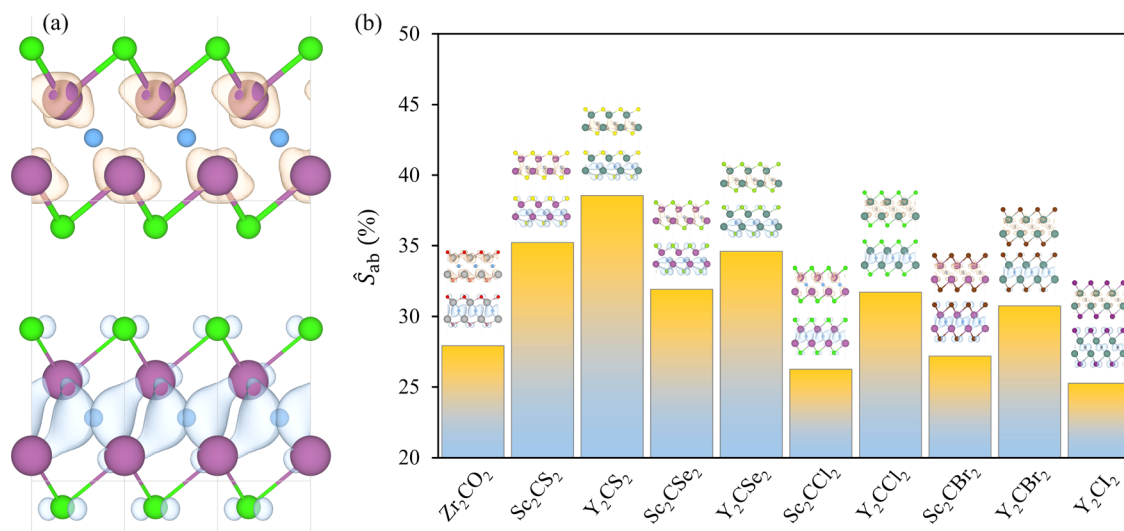

Fig. 8 (a) VBM (blue) and CBM (orange) partial charge densities for the Sc_2CCl_2 terminated MXene, at an isovalue of 0.01e Å^{-3}. (b) Spatial overlap, $\hat{S}_{ab}$, percentage between the VBM and CBM charge densities for the promising MXenes.

3310 | J. Mater. Chem. A, 2025, **13**, 3302–3316

This journal is © The Royal Society of Chemistry 2025

present larger overlaps, exceeding 30%, with the highest overlap observed in Y_2CS_2. In general, Y-MXenes exhibit greater overlap compared to their Sc-MXene counterparts, likely due to the larger size of Y atoms and the more diffuse nature of their 4d orbitals compared to the 3d orbitals of Sc. In terms of the distorted cases, see Fig. S6 of the ESI,† the deformation benefits the spatial separation of charge densities, as indicated by the significantly reduced overlap percentages. The broken symmetry enables a new charge redistribution, which appears to favour the separation between the VBM and CBM.

In thin 2D monolayer materials like the MXenes studied here, achieving effective charge separation is challenging. This difficulty is why many researchers couple these materials with other semiconductors to form heterojunctions that better separate charges.[67] Still, the observed localization in different layers and low overlapping percentage of the VBM and CBM charge densities is a notable finding.

3.5. Charge carriers mobility

A photoinduced electron/hole pair will drift for a certain average lifetime before recombining. To ensure efficient photocatalysis, it is crucial to have a prolonged average lifetime for the charge carriers. This requires effective separation of the

photogenerated electron and hole pairs to prevent rapid recombination. The separation is influenced by the relative mobilities of the electron and hole. Consequently, semiconductors with unequal electron and hole mobility often offer longer charge carriers lifetimes. Furthermore, a system with direction-dependent mobility can further facilitate charge carrier separation.

The charge carrier mobilities for the electrons and holes have been calculated and listed in Table 3, along with their corresponding effective masses, elastic constants, and deformation potentials needed in their calculation, *vide supra*. These values were calculated along two perpendicular directions, x and y, which correspond to the *zigzag* and *armchair* directions, as stated in the computational details. As observed in the bandstructures from Fig. 5, two bands converge at the VBM, providing the created hole with two distinct migration channels. This dual-channel system implies the consideration of both valence bands in terms of charge carrier mobility. Consequently, the hole migrating through the valence band with lesser **k**-space curvature is referred to as the heavy hole, h^H, while the one migrating through the more curved valence band is denoted as the light hole, h^L. An example of the fittings used to obtain the C_{2D} and E_d parameters is given in Fig. S7 of the

Table 3 Charge carrier properties for the non-distorted MXenes, where m_i^* is the carrier effective mass along the i transport direction, as a fraction w.r.t to a free electron. $C_{2D,i}$ is the elastic constant in i transport direction in units of N m^{-1}, $E_{d,i}$ is the deformation potential constant, given in eV, and μ_i is the carrier mobility, in cm^2 V^{-1} s^{-1} at $T = 300$ K. The e, h^H, and h^L carriers denote the electron, heavy hole, and light hole, respectively

MXene	Carrier	m_x^*	m_y^*	$C_{2D,x}$	$C_{2D,y}$	$E_{d,x}$	$E_{d,y}$	μ_x	μ_y
Zr_2CO_2	e	0.27	2.11			10.94	4.92	244.97	148.99
	h^H	0.43	0.43	274.39	267.44	5.95	6.25	898.22	782.72
	h^L	0.19	0.19			0.95	1.31	183 662.10	93 597.25
Sc_2CS_2	e	3.42	2.55			−2.25	−1.38	34.80	125.75
	h^H	0.72	0.73	83.64	84.47	4.73	4.61	152.08	159.70
	h^L	0.44	0.44			−0.31	−0.52	96 182.33	33 884.35
Y_2CS_2	e	1.85	1.95			−1.41	−0.82	193.54	535.00
	h^H	0.82	0.82	63.24	63.19	7.02	7.06	40.39	39.75
	h^L	0.55	0.55			2.16	2.50	959.91	712.61
Sc_2CSe_2	e	2.02	2.04			2.06	−0.74	92.90	707.25
	h^H	0.60	0.60	76.02	75.21	2.97	2.85	510.77	547.71
	h^L	0.31	0.32			−3.83	−3.78	1118.25	1126.69
Y_2CSe_2	e	5.01	1.55			3.80	1.42	6.04	140.46
	h^H	0.73	0.74	57.10	57.25	5.00	4.95	90.94	91.69
	h^L	0.43	0.43			−0.83	−0.72	9766.42	12 839.73
Sc_2CCl_2	e	0.25	1.19			1.58	1.38	9042.74	2488.56
	h^H	1.77	1.77	147.82	145.27	1.20	1.15	692.65	747.72
	h^L	0.42	0.41			−4.19	−4.17	1031.93	1042.20
Y_2CCl_2	e	0.23	0.96			3.46	2.88	1978.55	684.51
	h^H	3.74	3.81	121.33	121.19	2.98	2.85	20.60	22.08
	h^L	0.50	0.50			−2.32	−2.50	1905.93	1640.70
Sc_2CBr_2	e	0.25	1.22			1.87	1.34	6487.19	2537.44
	h^H	1.09	1.09	143.19	142.30	1.02	0.61	2503.32	6827.16
	h^L	0.30	0.30			−5.71	−5.51	1061.61	1142.40
Y_2CBr_2	e	0.22	0.96			1.76	2.10	7972.61	1278.38
	h^H	2.34	2.40	120.57	118.26	1.64	1.64	171.43	165.57
	h^L	0.41	0.41			−3.42	−3.35	1289.80	1328.13
Y_2CI_2	e	0.21	1.02			1.08	1.01	21 368.14	5259.49
	h^H	0.83	0.85	112.50	118.79	−0.75	−0.90	6003.60	4360.91
	h^L	0.22	0.22			−6.26	−6.35	1250.76	1301.68

This journal is © The Royal Society of Chemistry 2025
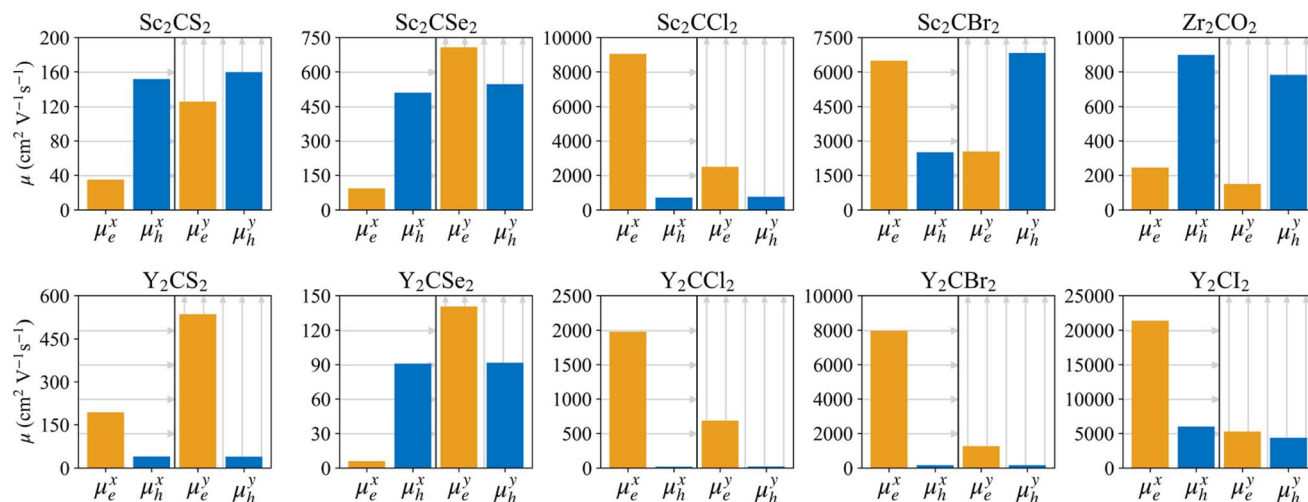
J. Mater. Chem. A, 2025, **13**, 3302–3316 | **3311**

Fig. 9 Charge carrier mobility, μ, in cm^2 V^{-1} s^{-1}, for the electrons and heavy holes along the x (*zigzag*) and y (*armchair*) directions for the regular MXenes. The orange and blue bars indicate, respectively, the electron and heavy hole mobilities.

ESI† for the example of Y$_2$CCl$_2$. To provide a more visual representation of the mobilities between e–h and their directionality, we have also represented these values as a bar plot in Fig. 9.

In general, the mobility of electrons in MXenes varies significantly depending on the x or y direction. For the S- and Se-terminated MXenes, with an H$_{MX}$ structure, electron mobility is higher along the y-direction compared to the x-direction, while, for the rest, displaying H$_M$ structures, this trend is reversed, presenting higher electron mobilities along the x-direction. Despite these directional differences in electron mobility, heavy holes tend to maintain consistent mobility across both directions, with the exception of the Sc$_2$CBr$_2$ system, where the heavy holes are more mobile in the y-direction. This exceptionality in Sc$_2$CBr$_2$ actually makes it particularly effective for charge separation, as it demonstrates both a significant disparity in electron and hole mobilities within the same direction and a clear direction-dependent mobility, with electrons favoring migration along the x-direction while holes prefer the y-direction. The other halide-terminated MXenes also deserve attention due to their large electron–hole mobility disparities, especially along the x-direction where electrons typically have higher mobilities. A similar pattern is observed in the Zr$_2$CO$_2$ MXene, although in this case, the holes are the ones exhibiting higher mobilities.

Light holes, while not necessarily the preferred pathway for hole migration due to the tendency of holes to occupy higher energy bands, in this case heavy holes, still play an important role in the overall charge carrier dynamics and need to be considered. These light holes exhibit significantly higher mobilities compared to the heavy ones, often by orders of magnitude, due to their lower effective masses and reduced deformation potentials. Notable exceptions to this trend are found in Y$_2$CI$_2$ and Sc$_2$CBr$_2$ MXenes. The higher mobility of light holes further facilitates charge separation, particularly in materials such as Zr$_2$CO$_2$, Sc$_2$CS$_2$, and Y$_2$CSe$_2$, where the

significant imbalance between the electron and light-hole mobilities enhances the effectiveness of charge separation. In the distorted phases of the S- and Se-terminated MXenes, see Table S1 and Fig. S8 of the ESI,† the mobility values differ slightly, but the general trends and ratios remain consistent with the non-distorted structures. Electrons tend to have higher mobilities in the x-direction than in the y-direction, heavy holes maintain relatively isotropic mobilities, and light holes continue to exhibit greater anisotropy and higher mobility values.

Despite the growing interest in MXenes due to their promising photocatalytic applications, the literature on the charge carrier mobilities of these materials remains relatively sparse. Among the various MXenes explored, the majority have not yet been comprehensively studied in this regard, underscoring the novelty and significance of the present computational investigation. To date, detailed mobility data are primarily available only for Zr$_2$CO$_2$ and Sc$_2$CCl$_2$ MXenes.[17,51,67–71] Even if reported mobility values for these MXenes vary somewhat across different studies, the overall trends and directionality of charge carriers remain consistent both within these studies and in comparison to our findings. Notably, our results align particularly well with those reported in ref. 51 for Sc$_2$CCl$_2$ and ref. 67 for Zr$_2$CO$_2$.

One might consider that the IEF of the S- and Se-terminated MXenes may influence mobility, however, in this case, the IEF is oriented along the z-direction, meaning it does not directly affect the present mobility values calculated in the x and y directions. Nevertheless, the presence of the IEF is critical for enhancing the separation of photogenerated electrons and holes across the two surfaces of the MXenes, thereby facilitating the charge separation. To estimate the intensity of the IEF, we calculated the electrostatic potential difference ($\Delta\phi$) between the two surfaces of the MXenes. The IEF can then be expressed as $E_{IEF} = \Delta\phi/ed$, as previously used for other Y-based Janus MXenes.[18] For the regular Sc$_2$CS$_2$, Y$_2$CS$_2$, Sc$_2$CSe$_2$, and Y$_2$CSe$_2$

3312 | *J. Mater. Chem. A*, 2025, **13**, 3302–3316

This journal is © The Royal Society of Chemistry 2025

MXenes, the obtained IEF values, in V Å^{-1}, are 0.26, 0.17, 0.24, and 0.18, respectively. The distorted phases yield similar IEF values of 0.27, 0.25, 0.25, and 0.21 V Å^{-1}, respectively. Overall, the distorted structures exhibit slightly higher IEF values, with Sc-MXenes showing greater values compared to Y-MXenes in both the regular and distorted cases.

3.6. Optical properties

Optical absorption is another crucial factor influencing the photocatalytic effectiveness of a material. An effective photocatalyst must be capable of absorbing a substantial portion of either visible or UV light—the primary components of solar radiation—, efficiently converting this absorbed light into hole–electron photogenerated pairs, which eventually separate and promote the photocatalytic process. Here, we explored the light harvesting properties of the studied MXenes by determining the optical absorption coefficient, see Fig. 10, derived from the dielectric functions, see Fig. S9 of the ESI.† Our calculations showed very low ε_{zz} components, a common feature in 2D materials,[72] so the results presented and discussed are from in-plane polarization $(\varepsilon_{xx} + \varepsilon_{yy})/2$, parallel to the MXene xy plane.

Most MXenes demonstrate good absorption in the visible spectrum, around 10^5 cm^{-1} in all cases, with the first absorption peak occurring within the visible region. However, some S- and Se-terminated MXenes exhibit a slight shift into the UV range, corresponding to their slightly larger bandgaps. The optical gaps, including excitonic effects calculated using the GW-BSE formalism, are listed in Table 2. Notably, even if Y-based MXenes typically have similar or even larger electronic bandgaps compared to Sc-based ones, their corresponding optical gaps are consistently smaller. When distorted, the electronic bandgap diminishes, and so does the optical gap, making these structures slightly more efficient with visible light absorption. From the GW-BSE optical spectra and the minimum direct electronic bandgap transition, the exciton binding energy can be estimated, shown in Table 2. This value represents the energy required to dissociate an exciton into its constituent electron and hole

Table 4 Parameters for the STH efficiency estimate, with $\Delta\phi$ being the difference between the vacuum energies at the two MXene surfaces for Janus cases, χ_{H_2} and χ_{O_2} being the HER and OER overpotentials at pH = 0, respectively, all given in eV, and η_{abs}, η_{cu}, η_{STH} and η'_{STH} representing the efficiency of light absorption, carrier utilization, STH, and corrected STH, respectively, given in percentage

MXene	$\Delta\phi$	χ_{H_2}	χ_{O_2}	η_{abs}	η_{cu}	η_{STH}	η'_{STH}
Zr$_2$CO$_2$	0.00	0.53	0.51	8.3	30.3	2.5	2.5
Sc$_2$CS$_2$	1.20	1.77	1.44	2.6	34.4	0.9	0.9
Y$_2$CS$_2$	0.83	1.89	1.13	7.2	37.8	2.7	2.7
Sc$_2$CSe$_2$	1.19	1.76	0.95	4.1	35.7	1.5	1.4
Y$_2$CSe$_2$	0.91	1.86	1.04	6.2	37.2	2.3	2.3
Sc$_2$CCl$_2$	0.00	0.22	1.03	24.6	44.9	11.0	11.0
Y$_2$CCl$_2$	0.00	0.35	0.86	41.8	50.8	21.3	21.3
Sc$_2$CBr$_2$	0.00	0.37	0.72	24.2	44.8	10.9	10.9
Y$_2$CBr$_2$	0.00	0.36	0.77	43.8	51.5	22.6	22.6
Y$_2$CI$_2$	0.00	0.56	0.15	46.6	26.2	12.2	12.2
d-Sc$_2$CS$_2$	1.31	1.76	1.32	7.3	37.9	2.8	2.7
d-Y$_2$CS$_2$	1.24	1.95	1.26	13.4	40.8	5.5	5.2
d-Sc$_2$CSe$_2$	1.29	1.57	1.05	16.7	42.1	7.0	6.5
d-Y$_2$CSe$_2$	1.14	1.70	1.14	13.4	40.8	5.5	5.2

charge carriers, providing insights into the ease of charge separation. The E_b values for regular structured MXenes are mostly comprised between 0.4 and 0.6 eV, similar to those found in other reported MXenes and transition metal dichalcogenides,[42] with Sc$_2$CSe$_2$ and Y$_2$CSe$_2$ breaking that rule with values of 0.33 eV and 0.74 eV, respectively. Regarding the distorted MXenes, Sc$_2$CS$_2$ becomes the system with lowest E_b (0.29 eV), while Y-based MXenes present values over 0.6 eV. In this sense, the most promising materials are those with the lowest E_b, as they facilitate the easiest dissociation of excitons. This makes regular Sc$_2$CSe$_2$ and distorted Sc$_2$CS$_2$ MXenes most optimal among the studied systems.

The STH conversion efficiency is also an important parameter when evaluating the efficiency of converting solar energy into hydrogen fuel for the water-splitting reaction. Here the
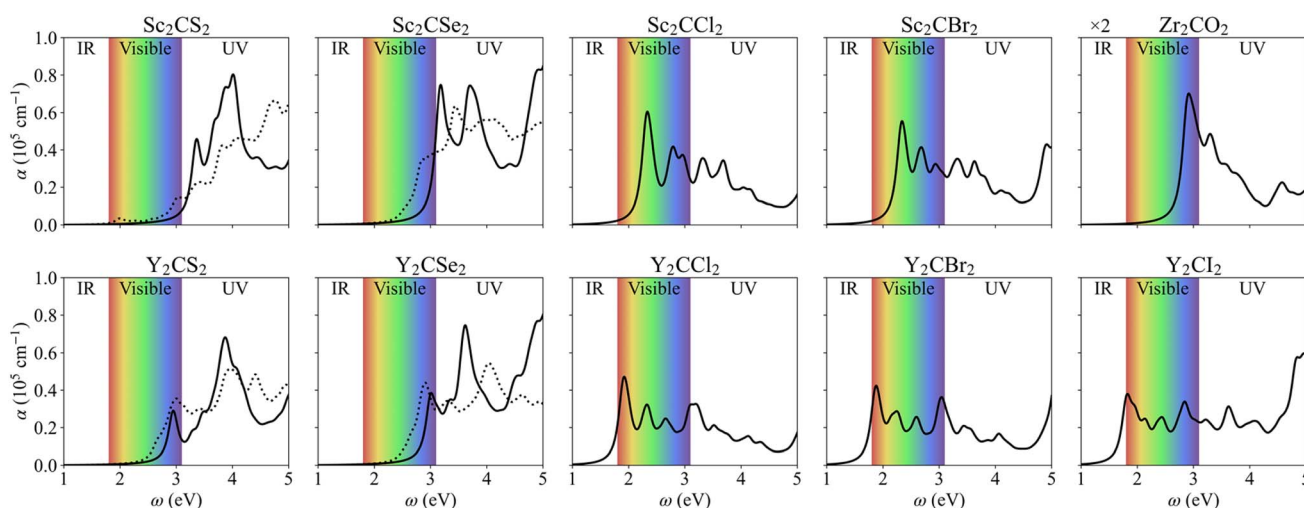
Fig. 10 Optical absorption coefficient, α, in 10^5 cm^{-1}, as a function of the photon energy, ω, in eV. The dotted lines in the chalcogen-terminated MXenes represent the distorted structure values. The Zr$_2$CO$_2$ values have been scaled down by half for comparison purposes.

This journal is © The Royal Society of Chemistry 2025

J. Mater. Chem. A, 2025, **13**, 3302–3316 | **3313**

upper limit of the STH efficiency has been estimated at pH = 0 and 7. The results at pH = 0 are encompassed in Table 4, and show that the light absorption efficiency, η_{abs}, of the studied 2D materials have a close relationship with their bandgap, in that a bandgap increase is accompanied by a decrease in light absorption efficiency. The halide-terminated Y-based MXenes exhibit the highest absorption efficiency and carrier utilization efficiency, resulting in superior STH efficiencies ranging from 21 to 23% for Cl- and Br-terminated structures. Notably, Y_2CI_2 presents the worst STH efficiency among the halide-terminated Y-MXenes due to its low OER overpotential and carrier utilization, however, its high absorption efficiency compensates this, leading to an STH efficiency of 12.2%. Sc-based MXenes with halide terminations follow closely, achieving an STH efficiency around 11%. Finally, the chalcogen-terminated MXenes, due to their large optical gap, show low absorption and STH efficiencies, not exceeding 3%. Nevertheless, in their distorted phases, the reduced bandgap enhances the absorption efficiency and so raises STH efficiencies up to 6.5%. The intrinsic electric field correction has minimal impact on both regular and distorted Janus S- and Se-MXenes. At pH = 7, as detailed in Table S2 of the ESI,† the Cl- and Br-terminated MXenes lose their photocatalytic ability for the HER, making STH calculation not possible. The other cases remain unaffected, except for Y_2CI_2, where the adjusted overpotentials improve the carrier utilization, increasing STH efficiency to 21.4%.

Overall, the most favourable solar-to-hydrogen efficiency is found for halide-terminated Y-MXenes, with STH values comparable to other Y-based MXenes,[18] and considerably higher than WX_2 (X = S, Se), which top at 9%.[73]

4. Conclusions

In the present study, first-principles calculations were employed to investigate the photoactive properties of a selection of ten MXenes—Zr_2CO_2, Sc_2CT_2, Y_2CT_2 (T = Cl, Br, S, and Se), and Y_2CI_2—in the context of water splitting. Distorted phases for the S- and Se-terminated MXenes were also considered and were found to exhibit properties that were generally very similar to their regular counterparts. Based on their cohesive and formation energies, and phonons spectra, this subset of MXenes are found to be energetically and dynamically stable. All the selected MXenes are also shown to be semiconductors with an indirect bandgap that falls within the visible or near UV range (the latter for chalcogen-terminated cases), making them suitable for photocatalysis.

Moreover, their band alignment is appropriate for water splitting photocatalysis. This band alignment can be adjusted by pH changes, with the HER reaction being switched off at pH = 7 for halide-terminated MXenes. The intrinsic electric field in the H_{MX} S- and Se-terminated Janus structures enhances charge carrier separation by accumulating electrons on the H_X face and holes on the H_M face. Typically, the VBM of the studied MXenes is distributed along the p orbitals of the C atoms, with minor contributions from the p orbitals of the terminations, while the CBM is primarily centered around the TM layers. The selected MXenes present good properties for charge carrier separation, with MXenes presenting a disparity between the electrons and hole mobilities, with electrons showing anisotropic mobilities. Moreover, in Sc_2CBr_2, we found direction-dependent mobilities, with electrons favoring migration along the x-direction and holes preferring the y-direction.

These MXenes possess an optical gap that falls within the optimal range of the solar spectrum for efficient light absorption, while also sufficiently wide to provide the necessary photogenerated energy to overcome the potential barrier for water splitting, as evidenced by the optical absorption and STH efficiency calculations. Achieving spatial separation of charge density in thin 2D materials is challenging, and the VBM and CBM overlap values of around 30%, along with the somewhat high exciton binding energies observed in the studied MXenes, may act as inhibitors to their optimal photocatalytic effectiveness. However, MXenes can be coupled with other 2D materials to form heterojunctions, which have been shown to reduce exciton binding energies and further separate the VBM and CBM states.[71]

Accordingly with the exhibited results, the presented MXenes show promising properties for high-performance photocatalytic water splitting. In particular, the halide-terminated MXenes and Zr_2CO_2 demonstrate superior properties compared to the chalcogen-terminated variants. These include greater stability, enhanced absorption in the visible light range, reduced charge density overlap, improved charge carrier mobility, and higher STH efficiency. The present research can provide insightful and helpful information, laying the grounds for future computational and experimental design of MXene-based photocatalysts. Indeed, the findings of this study provide a strategic guide for future experimental research on MXenes for photocatalytic water splitting. By identifying MXenes with optimal band alignment, robust stability, and high solar-to-hydrogen efficiency potential, this theoretical framework narrows down the selection of candidates for synthesis and testing. The calculated bandgaps and charge carrier mobilities for the proposed optimal MXene compositions offer key parameters that can be used to refine synthesis conditions, modify terminations, or engineer heterostructures to enhance photocatalytic performance.

Data availability

The data supporting this article have been included as part of the ESI.†

Conflicts of interest

The authors declare no competing financial interest.

Acknowledgements

3314 | J. Mater. Chem. A, 2025, **13**, 3302–3316

This journal is © The Royal Society of Chemistry 2025

References

1 N. S. Lewis, *Science*, 2007, **315**, 798–801.

2 D. Larcher and J. M. Tarascon, *Nat. Chem.*, 2015, **7**, 19–29.

3 J. A. Turner, *Science*, 2004, **305**, 972–974.

4 G. Squadrito, G. Maggio and A. Nicita, *Renewable Energy*, 2023, **216**, 119041.

5 K. Maeda and K. Domen, *J. Phys. Chem. Lett.*, 2010, **1**, 2655–2661.

6 T. Hisatomi and K. Domen, *Nat. Catal.*, 2019, **2**, 387–399.

7 Á. Morales-García, F. Viñes, C. Sousa and F. Illas, *J. Phys. Chem. Lett.*, 2023, **14**, 3712–3720.

8 Q. Zhong, Y. Li and G. Zhang, *Chem. Eng. J.*, 2021, **409**, 128099.

9 Y. Gogotsi, *Chem. Mater.*, 2023, **35**, 8767–8770.

10 B. Anasori and Y. Gogotsi, *Graphene 2D Mater.*, 2023, **8**, 39–41.

11 M. Naguib, M. Kurtoglu, V. Presser, J. Lu, J. Niu, M. Heon, L. Hultman, Y. Gogotsi and M. W. Barsoum, *Adv. Mater.*, 2011, **23**, 4248–4253.

12 M. Alhabeb, K. Maleski, B. Anasori, P. Lelyukh, L. Clark, S. Sin and Y. Gogotsi, *Chem. Mater.*, 2017, **29**, 7633–7644.

13 M. Naguib, O. Mashtalir, J. Carle, V. Presser, J. Lu, L. Hultman, Y. Gogotsi and M. W. Barsoum, *ACS Nano*, 2012, **6**, 1322–1331.

14 M. A. Hope, A. C. Forse, K. J. Griffith, M. R. Lukatskaya, M. Ghidiu, Y. Gogotsi and C. P. Grey, *Phys. Chem. Chem. Phys.*, 2016, **18**, 5099–5102.

15 V. Kamysbayev, A. S. Filatov, H. Hu, X. Rui, F. Lagunas, D. Wang, R. F. Klie and D. V. Talapin, *Science*, 2020, **369**, 979–983.

16 H. Ding, Y. Li, M. Li, K. Chen, K. Liang, G. Chen, J. Lu, J. Palisaitis, P. O. Å. Persson, P. Eklund, L. Hultman, S. Du, Z. Chai, Y. Gogotsi and Q. Huang, *Science*, 2023, **379**, 1130–1135.

17 Z. Guo, J. Zhou, L. Zhu and Z. Sun, *J. Mater. Chem. A*, 2016, **4**, 11446–11452.

18 S. Y. Zhang, N. P. Shi, C. K. Wang and G. P. Zhang, *Phys. Chem. Chem. Phys.*, 2024, **26**, 412–420.

19 D. Ontiveros, F. Viñes and C. Sousa, *J. Mater. Chem. A*, 2023, **11**, 13754–13764.

20 D. Ontiveros, S. Vela, F. Viñes and C. Sousa, *Energy Environ. Mater.*, 2024, **7**, e12774.

21 Y. M. Ding, X. Nie, H. Dong, N. Rujisamphan and Y. Li, *Nanoscale Adv.*, 2020, **2**, 2471–2477.

22 J. H. Liu, X. Kan, B. Amin, L. Y. Gan and Y. Zhao, *Phys. Chem. Chem. Phys.*, 2017, **19**, 32253–32261.

23 S. Guo, H. Lin, J. Hu, Z. Su and Y. Zhang, *Materials*, 2021, **14**, 4739.

24 C. Ougherb, T. Ouahrani, M. Badawi and Á. Morales-García, *Phys. Chem. Chem. Phys.*, 2022, **24**, 7243–7252.

25 A. Jurado, Á. Morales-García, F. Viñes and F. Illas, *J. Phys. Chem. C*, 2021, **125**, 26808–26813.

26 P. Hohenberg and W. Kohn, *Phys. Rev.*, 1964, **136**, 864–871.

27 W. Kohn and L. J. Sham, *Phys. Rev.*, 1965, **140**, 1133–1138.

28 G. Kresse and J. Hafner, *Phys. Rev. B: Condens. Matter Mater. Phys.*, 1994, **47**, 558–561.

29 J. P. Perdew, K. Burke and M. Ernzerhof, *Phys. Rev. Lett.*, 1996, **77**, 3865–3868.

30 J. P. Perdew and W. Yue, *Phys. Rev. B: Condens. Matter Mater. Phys.*, 1986, **33**, 8800–8802.

31 C. Adamo and V. Barone, *J. Chem. Phys.*, 1999, **110**, 6158–6170.

32 X. Hai, J. Tahir-Kheli and W. A. Goddard III, *J. Phys. Chem. Lett.*, 2011, **2**, 212–217.

33 P. E. Blöchl, *Phys. Rev. B: Condens. Matter Mater. Phys.*, 1994, **50**, 17953–17979.

34 H. J. Monkhorst and J. D. Pack, *Phys. Rev. B: Solid State*, 1976, **13**, 5188–5192.

35 V. Blum, R. Gehrke, F. Hanke, P. Havu, V. Havu, X. Ren, K. Reuter and M. Scheffler, *Comput. Phys. Commun.*, 2009, **180**, 2175–2196.

36 A. Togo and I. Tanaka, *Scr. Mater.*, 2015, **108**, 1–5.

37 X. Gonze and C. Lee, *Phys. Rev. B: Condens. Matter Mater. Phys.*, 1997, **55**, 10355–10368.

38 S. Trasatti, *Pure Appl. Chem.*, 1986, **58**, 955–966.

39 S. H. Mir, V. K. Yadav, J. K. Singh and J. K. Singh, *ACS Omega*, 2020, **5**, 14203–14211.

40 M. S. Hybertsen and S. G. Louie, *Phys. Rev. B: Condens. Matter Mater. Phys.*, 1986, **34**, 5390–5413.

41 S. Albrecht, L. Reining, R. Del Sole and G. Onida, *Phys. Rev. Lett.*, 1998, **80**, 4510–4513.

42 Z. Jiang, Z. Liu, Y. Li and W. Duan, *Phys. Rev. Lett.*, 2017, **118**, 266401.

43 C. F. Fu, J. Sun, Q. Luo, X. Li, W. Hu and J. Yang, *Nano Lett.*, 2018, **18**, 6312–6317.

44 C. A. Gueymard, D. Myers and K. Emery, *Sol. Energy*, 2002, **73**, 443–467.

45 Y. Zheng, Y. Jiao, M. Jaroniec and S. Z. Qiao, *Angew. Chem.*, 2014, **54**, 52–65.

46 C. C. L. McCrory, S. Jung, J. C. Peters and T. F. Jaramillo, *J. Am. Chem. Soc.*, 2013, **135**, 16977–16987.

47 H. Zhu, N. Qiu, G. Fang and S. Du, *RSC Adv.*, 2023, **13**, 21690–21702.

48 L. Zhang, C. Tang, C. Zhang and A. Du, *Nanoscale*, 2020, **12**, 21291–21298.

49 M. Li, O. Omisakin and J. Young, *Nanoscale*, 2022, **14**, 6970–6980.

50 M. Khazaei, M. Arai, T. Sasaki, C.-Y. Chung, N. S. Venkataramanan, M. Estili, Y. Sakka and Y. Kawazoe, *Adv. Funct. Mater.*, 2013, **23**, 2185–2192.

51 L. Zhou, Y. Zhang, Z. Zhuo, A. J. Neukirch and S. Tretiak, *J. Phys. Chem. Lett.*, 2018, **9**, 6915–6920.

This journal is © The Royal Society of Chemistry 2025

J. Mater. Chem. A, 2025, **13**, 3302–3316 | **3315**

52 S. J. Hwu, R. P. Ziebarth, S. von Winbush, J. E. Ford and J. D. Corbett, *Inorg. Chem.*, 1986, **25**, 283–287.

53 H. Shin, S. Kang, J. Koo, H. Lee, J. Kim and Y. Kwon, *J. Chem. Phys.*, 2014, **140**, 114702.

54 H. M. Shodja, F. Ojaghnezhad, A. Etehadieh and M. Tabatabaei, *Mech. Mater.*, 2017, **110**, 1–15.

55 F. Ersan, E. Aktürk and S. Ciraci, *Phys. Rev. B*, 2016, **94**, 245417.

56 P. Hess, *Nanoscale Horiz.*, 2021, **6**, 856–892.

57 Y. Jiang, Y. Zhang, Q. Huang, L. Hao and S. Du, *J. Mater. Res. Technol.*, 2020, **9**, 14979–14989.

58 K. Gaál-Nagy, *Phys. Rev. B: Condens. Matter Mater. Phys.*, 2008, **77**, 024309.

59 I. Pallikara, P. Kayastha, J. M. Skelton and L. D. Whalley, *Electron. Struct.*, 2022, **4**, 033002.

60 V. Wang, G. Tang, Y. C. Liu, R. T. Wang, H. Mizuseki, Y. Kawazoe, J. Nara and W. T. Geng, *J. Phys. Chem. Lett.*, 2022, **13**, 11581–11594.

61 J. D. Gouveia and J. R. B. Gomes, *Phys. Rev. Mater.*, 2022, **6**, 024004.

62 H. Liang and J. Liu, *ChemCatChem*, 2022, **14**, e202101375.

63 T. Su, X. Ma, J. Tong, H. Ji, Z. Qin and Z. Wu, *J. Mater. Chem. A*, 2022, **10**, 10265–10296.

64 X. Zhang, J. X. Shen, W. Wang and C. G. Van De Walle, *ACS Energy Lett.*, 2018, **3**, 2329–2334.

65 S. A. Razek, M. R. Popeil, L. Wangoh, J. Rana, N. Suwandaratne, J. L. Andrews, D. F. Watson, S. Banerjee and L. F. J. Piper, *Electron. Struct.*, 2020, **2**, 023001.

66 E. S. Sim, H. Nam, C. Kim and Y. C. Chung, *Sustainable Mater. Technol.*, 2022, **34**, e00502.

67 X. Xu, X. Wu, Z. Tian, M. Zhang, L. Li and J. Zhang, *Appl. Surf. Sci.*, 2022, **599**, 154014.

68 R. Sun, C. L. Yang, M. S. Wang and X. G. Ma, *Appl. Surf. Sci.*, 2022, **591**, 153232.

69 Y. He, M. Zhang, J. J. Shi, Y. L. Cen and M. Wu, *J. Phys. Chem. C*, 2019, **123**, 12781–12790.

70 H. Zhang, G. Yang, X. Zuo, H. Tang, Q. Yang and G. Li, *J. Mater. Chem. A*, 2016, **4**, 12913–12920.

71 R. Zhang, F. Zhuang, R. Zhou, J. Ma, H. Li, K. Wang, X. Ye and G. Hao, *J. Phys. Chem. Solids*, 2022, **171**, 111014.

72 T. Ketolainen and F. Karlicky, *J. Mater. Chem. C*, 2022, **10**, 3919–3928.

73 L. Ju, M. Bie, X. Tang, J. Shang and L. Kou, *ACS Appl. Mater. Interfaces*, 2020, **12**, 29335–29343.

3316 | *J. Mater. Chem. A*, 2025, **13**, 3302–3316

This journal is © The Royal Society of Chemistry 2025